

# **NDE of Solid Surfaces and Thin Surface Coatings by Means of Surface Brillouin Scattering of Light**

J. D. Comins, A. G. Every, P. R. Stoddart, W. Pang, and X. Zhang.  
Materials Physics Institute and School of Physics  
University of the Witwatersrand  
Wits 2050 Johannesburg  
South Africa

## **Abstract**

Surface Brillouin scattering of light is finding increasing use in surface characterization. It is a sensitive probe for measuring the near surface elastic properties of solids and surface coatings ranging in thickness from a few nanometers to a micron or so. The method is based on the small frequency shift that light, scattered from a surface undergoes, due to thermally excited dynamic surface corrugations and fluctuations in sub-surface strains. The observed spectra display prominent features due to Rayleigh and other guided surface modes. This paper will include a review of the Brillouin scattering technique and the modelling of Brillouin spectra on the basis of surface dynamic response functions. Results that have been obtained in our laboratory in a number of studies will be presented, including the measurement of the elastic constants of vanadium carbide and the nickel-based superalloy CMSX4 (the latter as a function of temperature) and two types of coatings, TiN on high speed steel (an example of a fast on slow combination) and amorphous silicon on silicon (a slow on fast system).

## **1. Introduction**

Surface Brillouin scattering (SBS) is now an established technique in the characterization of surfaces, interfaces and thin supported films [1-4] and it is being extended into the wider industrial arena. It has a major advantage of being able to determine elastic properties within the range from 10 to 1000 nm of a surface or interface and thus is suited to studies of thin protective coatings, near surface effects of radiation damage, polishing and other surface modifications. SBS involves the study of thermally induced surface acoustic excitations in the GHz frequency range and hence the elastic constants of opaque solids and thin supported layers. The advances in SBS followed the production of the high contrast ( $\sim 10^{12}$ ), multi-pass tandem Fabry-Pérot interferometer [1,2], and high-sensitivity low-noise detectors that have been complemented by the development of theoretical and computational methods using surface Green's functions. These have provided a detailed understanding of variety of acoustic excitations measured in the experiments. It is a non-contact technique having the advantage that small samples can be used and has been recently extended to high temperatures and pressures in our laboratory [8-12].

## **Theoretical and Experimental Aspects**

In SBS a laser beam is focussed onto the sample by a lens in the back-scattering arrangement shown in Fig.1. The wavevector  $\mathbf{k}_i$  of the incident light makes an angle  $\theta$  with the normal to the surface of the sample and the light back-scattered by a surface acoustic excitation (phonon) of wavevector  $\mathbf{k}_{//}$  into a small cone around  $\mathbf{k}_s = -\mathbf{k}_i$  is collected by the same lens. The application of wavevector conservation leads to the relationship

$$k_{//} = 2k_i \sin \theta. \quad (1)$$

The velocity of the surface acoustic excitation is  $v = \omega / k_{\parallel}$  where  $\omega$  is its the angular frequency. For a chosen incident wavelength of light (e.g. 514.5 nm), the angle of incidence  $\theta$  establishes  $k_{\parallel}$  while the measurement of  $\omega$  by the frequency shift of the scattered light from the incident laser frequency determines  $v$ . By rotating the sample about the normal to its surface by a given angle  $\alpha$  from a chosen symmetry direction (e.g. from the [100] direction on the (001) plane in a cubic material) the angular variation of the SAW velocities can be studied. The back-scattering geometry and its relationship to measurement precision in SBS experiments has been studied in detail by Stoddart et al. [13].

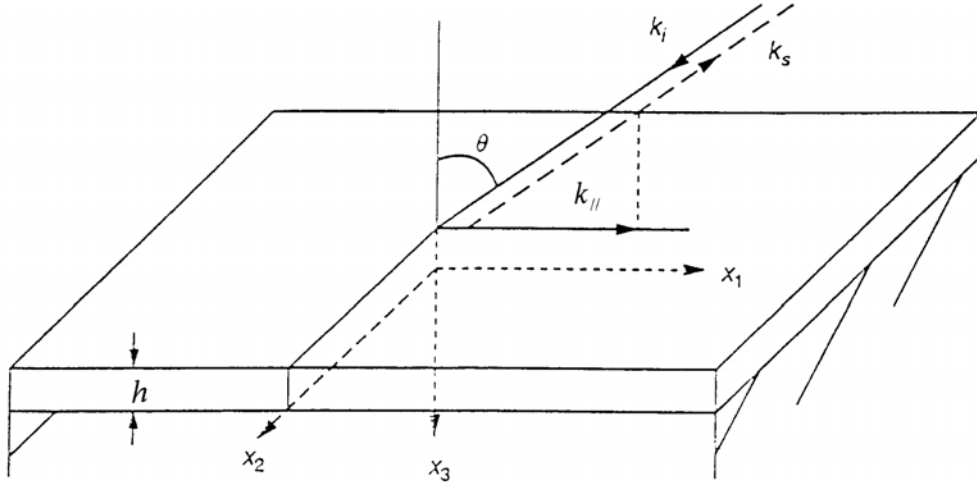


Fig. 1. The scattering geometry.

The SBS spectrum from an isotropic opaque solid normally consists of a relatively intense peak resulting from the Rayleigh surface acoustic wave (SAW) such that  $\omega_R = v_R k_{\parallel}$ . At higher frequencies extending from a threshold, there appears the much weaker “Lamb shoulder” that results the displacements of the sample surface from the coupling to the continuum of bulk modes. For the more complex cases of anisotropic solids and thin supported films additional excitations may be observed depending on the nature of the sample and the experimental conditions; these include various pseudo-SAWs, pre-Rayleigh and quasi-Rayleigh waves, Sezawa and pseudo-Sezawa waves, Lamb waves and interface excitations.

In opaque materials, light scattering by the surface ripple mechanism dominates that by elasto-optic coupling, and the frequency spectrum of the scattered light provides information on the surface dynamics and the near-surface elastic properties of the materials under investigation. For sufficiently high temperatures for which  $T \gg \hbar \omega / k_B$ , (e.g. room temperature), the scattering cross section  $I(\omega)$  for ripple scattering by a surface acoustic excitation of wavevector  $k_{\parallel}$  and angular frequency  $\omega$ , is proportional to the power spectrum of the normal displacements of the surface at that wavevector and angular frequency. The power spectrum is related to  $G_{33}$  the  $(x_3, x_3)$  component of the Fourier (angular frequency and wavevector) domain elasto-dynamic Green’s function evaluated at the surface. Thus

$$I(\omega) = A \frac{T}{\omega} \text{Im}[G_{33}(k_{//}, x_3 = 0, \omega + i0)] \quad (2)$$

where  $A$  is a constant that depends on the optical properties of the medium, the scattering geometry and the frequency and polarisation of the incident light.

The method of calculation of  $G_{33}$  has been described in detail by Zhang et al. [11]. As a brief illustration, consider SBS from a supported film as shown in Fig. 1. The calculation uses the method of partial waves that satisfy the boundary conditions. The partial waves correspond to different wave vector components  $k_3^{(n)}$  normal to the free surface being real or complex solutions of the sextic Christoffel characteristic equation. For the layer, all six phase matched plane waves ( $n = 1, 2, 3, \dots, 6$ ) are used, and in the substrate, as discussed in ref. [14], only the three outgoing plane waves ( $n = 7, 8, 9$ ) are retained. The outgoing waves are either homogeneous with  $k_3^{(n)}$  real and having ray vectors  $\mathbf{V} = \partial\omega / \partial \mathbf{k}$  directed into the interior of the substrate, or evanescent waves with  $\text{Im}(k_3^{(n)}) > 0$ , and having amplitudes that decrease into the interior. The solutions that satisfy the boundary conditions are constructed as a superposition of the relevant plane waves. The boundary conditions on the surface tractions and displacements provide nine equations for determining the partial wave amplitudes. The Green's function for the free surface of the layer is represented by the superposition of the six partial waves in the layer:

$$G_{33}(k_{//}, x_3 = -d, \omega) = \sum_{n=1}^6 \frac{i}{\omega} \frac{\text{adj}(\mathbf{B})_3^{(n)}}{|\mathbf{B}|} U_3^{(n)} \exp[-i k_3^{(n)} h]. \quad (3)$$

where  $\mathbf{B}$  is the boundary condition matrix,  $U_3$  is the component of the mode polarisation, and  $h$  is the film thickness.

For the case of the surface of a half-space the form of the Green's function is

$$G_{33}(k_{//}, \omega) = \sum_{n=1}^3 \frac{i}{\omega} \frac{\text{adj}(\mathbf{B})_3^{(n)}}{|\mathbf{B}|} U_3^{(n)}, \quad (4)$$

in which

$$B_l^{(n)} = \sum_{pq} C_{3lpq} U_p^{(n)} k_q^{(n)} / \omega. \quad (5)$$

Eq.(5) illustrates the relationship between the boundary value determinant  $|\mathbf{B}|$  and the elastic properties of the material in this simplest case.

For the free surface of a half-space, the nature of the excitations depends on the real or complex values of the wave-vectors  $k_3^{(n)}$  of the partial waves. At frequencies lower than the transverse bulk wave threshold, the three partial wave solutions have complex  $k_3^{(n)}$ . The superposition of these phase-matched evanescent waves results in the Rayleigh wave (RW), a true surface wave whose amplitude reduces essentially to zero within a few wavelengths from the surface and results in a narrow intense peak in the SBS spectrum. Such a surface wave arises from the vanishing of the boundary value determinant  $|\mathbf{B}|$ . Bulk acoustic waves travelling towards such a surface that have a component of displacement normal to the surface also contribute to the SBS spectrum. In the frequency range above the longitudinal wave threshold, all contributing modes, longitudinal and transverse are propagating bulk waves with real  $k_3^{(n)}$ . For frequencies between the transverse and longitudinal thresholds, there is a mixture of modes with both real and complex values of  $k_3^{(n)}$ . The contribution of the bulk

waves leads to a continuous band of excitations (Lamb shoulder) in which the longitudinal (L) and transverse (T) thresholds are observable in the SBS spectra. These limiting bulk waves correspond to ray vectors parallel to the surface and are known as lateral waves. The limiting frequencies are  $\omega_T = v_T k_{//}$  and  $\omega_L = v_L k_{//}$  for the transverse and longitudinal wave thresholds, respectively.

In the case of a thin layer on a substrate, again vanishing of the boundary value determinant  $|B|$  results in a sharp line in the spectrum, which for a very thin film is close to the Rayleigh wave velocity of the substrate. A wealth of different types of excitation can occur depending on the film thickness and the relative magnitudes of the elastic constants of the film and substrate. For a soft film on a hard substrate additional surface modes called Sezawa waves are drawn out from the continuum with increasing film thickness. For both hard and soft films one or more pseudo SAWs, corresponding to minima in  $|B|$  may exist in the Lamb shoulder. These are surface modes that have a bulk wave component that results in energy radiating into the substrate and leads to attenuation. Adaptation of the theory allows the treatment of anisotropic multilayers and two elastic half-spaces in contact and the resulting interface modes.

The usual instrument now used for Brillouin scattering is the high contrast multi-pass tandem Fabry-Pérot (FP) interferometer of the Sandercock type used with a low-noise, high sensitivity detector. Sandercock [1] and Mutti et al [2] deal with the theory and operation of the (3+3)-pass instrument.

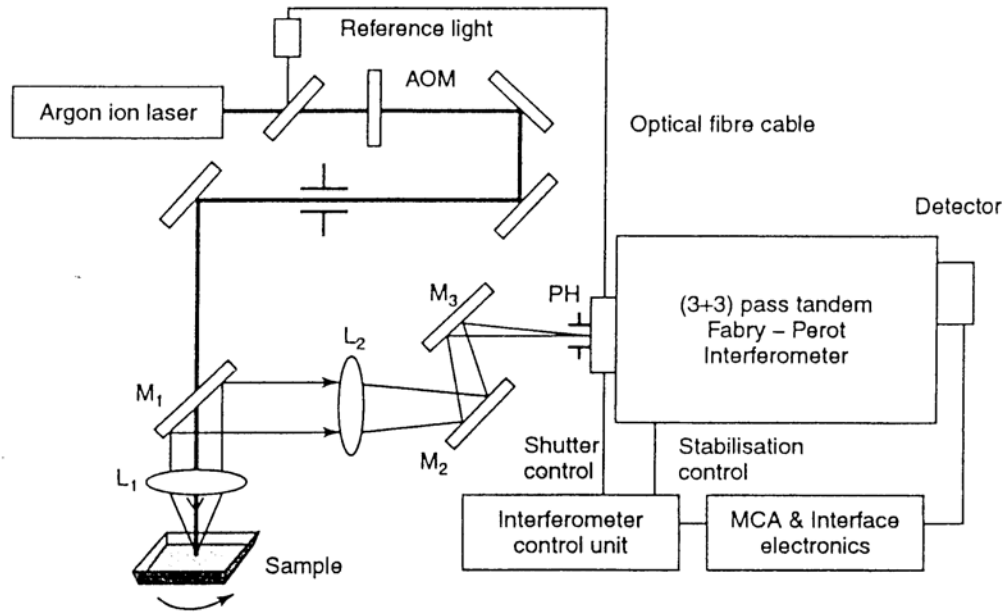


Fig. 2. Block diagram of experimental SBS arrangement

Fig.2 shows a block diagram of the tandem FP and the collection optics used in our laboratory. An electronically controlled vibration isolation system dynamically isolates the interferometer from the optical table. Light from an argon ion laser operated in a single axial mode is focussed by either a 50 mm or 120 mm focal length lens onto the sample. The scattered light is collected by the same lens and is directed by an elliptical mirror M1 with a central 2mm hole via steering mirrors M2 and M3 into the entrance pinhole of the

interferometer. The auxiliary optics includes a shutter system with an adjustable window period in which the elastically scattered light is prevented from entering the detector during each scan. During the window the shutter system provides the control signal necessary for automatic stabilization of the interferometer mirrors. The acousto-optic modulator allows the laser power on the sample to be continuously varied without affecting the control signal. An SPCM-PQ high quantum efficiency silicon avalanche photo-diode detector fitted with photon counting electronics was used and the signal were accumulated in the PC-based multichannel scalar.

## Results on various systems

### *Nickel-based superalloy CMSX-4*

Single crystal nickel-based superalloys are widely used in gas turbine engines since they retain useful strength at high temperatures. They have an interesting microstructure consisting of compositionally ordered fcc domains ( $\gamma'$  phase) embedded in a disordered fcc matrix ( $\gamma$  phase). In the sense that both phases share a common Bravais lattice, they form a single crystal.

In recent work by Zhang et al. [10], samples of CMSX-4 were cut, oriented by X-rays and mechanically polished to a surface finish of  $0.1\ \mu\text{m}$ . The collection lens had a focal length of 120 mm and an aperture of  $f/5.5$ . The incident angle  $\theta$  was 70.7 degrees determined by the geometry of the optical furnace used to provide the high temperatures.

There are several methods that have been employed to determine elastic constants for SBS measurements. We initially investigated the stability of the values extracted from the method of angular dependence of the SAW velocities for the (001) surface. As shown in Fig.3, two wave branches were observed: the Rayleigh SAW peak in the range 0 to 30 degrees from the [100] direction, while a pseudo-SAW (p-SAW) is present from 25 to 45 degrees from this direction. The latter excitation has two of its partial waves being evanescent while the third has a bulk-like nature. The p-SAW has a considerable surface character, but a shorter lifetime than the RW owing to energy losses to the bulk.

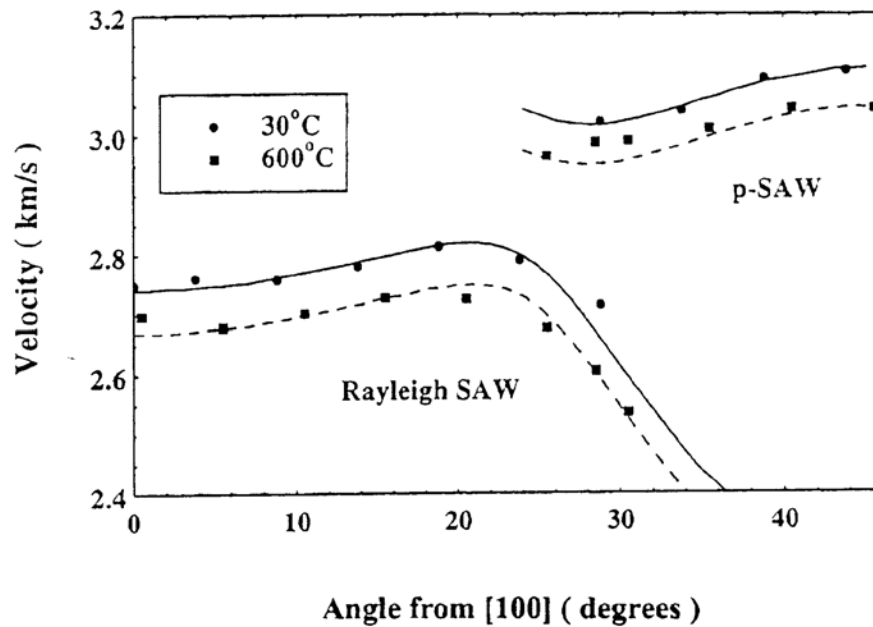


Fig. 3. Direction dependence of the Rayleigh and pseudo-SAW velocities for the nickel-based superalloy CMSX-4 at room temperature and 600 °C. The dispersion curves move to lower velocities as the temperature increases.

The angular dependence of the SAW velocities was determined for the (001) surface. Two wave branches were observed: the Rayleigh SAW peak in the range 0 to 30 degrees from the [100] direction, while the p-SAW is present from 25 to 45 degrees from this direction. The CMSX-4 superalloy is elastically highly anisotropic with anisotropy ratio  $A = 2.8$  and the velocities of the RW are strongly direction dependent. Moreover there is the presence of the PSAW to provided additional data. Nonetheless, attempts to extract the set of independent elastic constants ( $c_{11}$ ,  $c_{12}$  and  $c_{44}$ ) from the velocity dispersion of the RW and PSAW alone (as has been achieved in some cases) were unsuccessful and least-squares fitting procedures did not yield convergent values.

However, precise values of the elastic constants were recovered when the additional information provided by the Lamb shoulder was used,. The Rayleigh peak and the Lamb shoulder is shown in Fig. 4 for SBS spectra obtained for the [100] and [110] directions on the (001) surface of CMSX-4. The Rayleigh SAW results in the intense narrow peak, while at higher velocities, the details of the Lamb shoulder, while being much weaker than the RW are readily visible. The positions of the minima in the respective Lamb shoulders corresponding to the longitudinal thresholds are given by  $v_L = [(c_{11} + c_{12} + 2c_{44})/2\rho]^{1/2}$  for the [110] direction, while for the [100] direction  $v_L = (c_{11}/\rho)^{1/2}$ ; with no explicit solutions exist for the transverse wave thresholds in this case.

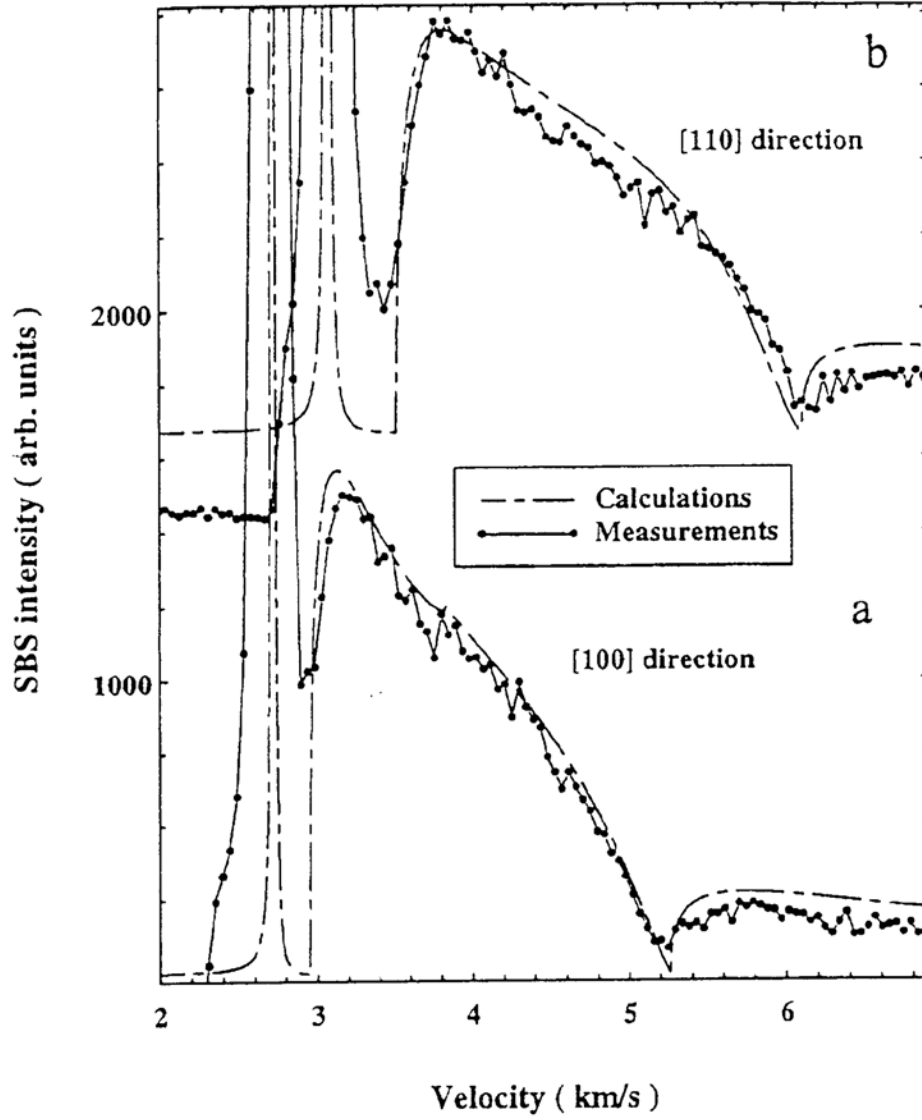


Fig. 4. The measured and calculated SBS spectra for the respective [100] and the [110] directions on the (001) surface for CMSX-4. The upper graph has been displaced for reasons of clarity.

These additional two measurements in combination with the SAW angular dispersion data shown in Fig.3 resulted in all three elastic constants being recovered successfully. The minimization of

$$\chi^2 = \sum_{SAWs} (V_i^{meas} - V_i^{calc})^2 + \sum_L (V_i^{meas} - V_i^{calc})^2$$

with respect to variations of the elastic constants was carried out, where the  $V_i^{calc}$  are the respective velocities determined from the surface Green's function for the RW and PSAW and the minimum in the Lamb continuum ( $L$ ). Fig. 5 shows the variation in  $\chi^2$  as a function of  $c_{11}$  and  $c_{44}$  for  $(c_{11} - c_{12}) = 90$  GPa. The minimum in  $\chi^2$  is well defined. The analysis yielded satisfactory ambient temperature elastic constants namely:  $c_{11} = 243 \pm 2$  GPa;  $c_{12} = 153 \pm 2$

GPa and  $c_{44} = 128 \pm 1$  GPa. A comparison of the experimental SBS spectra shows excellent agreement with those calculated by the surface Green's function (Fig. 4). It should be noted that the experimental RW peaks are instrumentally broadened.

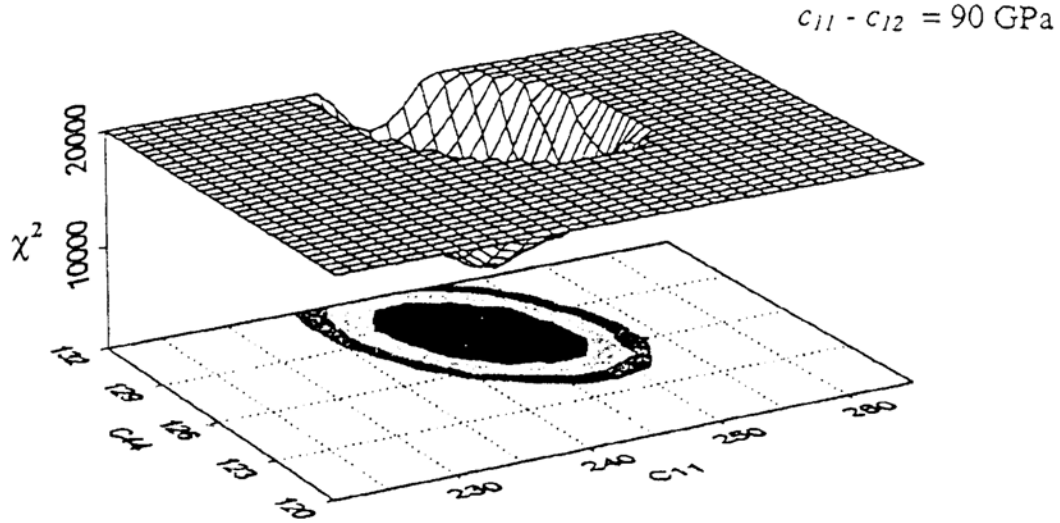


Fig. 5. Three dimensional graph of the variation of  $\chi^2$  with  $c_{11}$  and  $c_{12}$  for CMSX-4 using the combined data of the angular variation of SAW velocity and the Lamb shoulders. The elastic constant combination ( $c_{11} - c_{12}$ ) is pre-set to 90 GPa. The minimum is well-defined.

The elastic constants were measured as a function of temperature to 600 °C for CMSX-4 using an optical furnace that allowed the sample to be rotated about the surface normal. As discussed above, the room temperature measurements were obtained using the combined data from the SAW angular dispersion and the Lamb shoulder. The results at 200 and 400 °C were obtained for the [100] and [110] Lamb shoulder longitudinal threshold measurements alone. At 600 °C, owing to the deterioration of the surface only the angular dependence of the SAW velocities was measured, the details of the Lamb shoulder being too weak to determine with accuracy. As shown in Fig. 6, a linear decrease in the elastic constants with increasing temperature was observed in agreement with the quasi-harmonic theory, and demonstrates the self consistency of the methods used to determine the elastic constants.



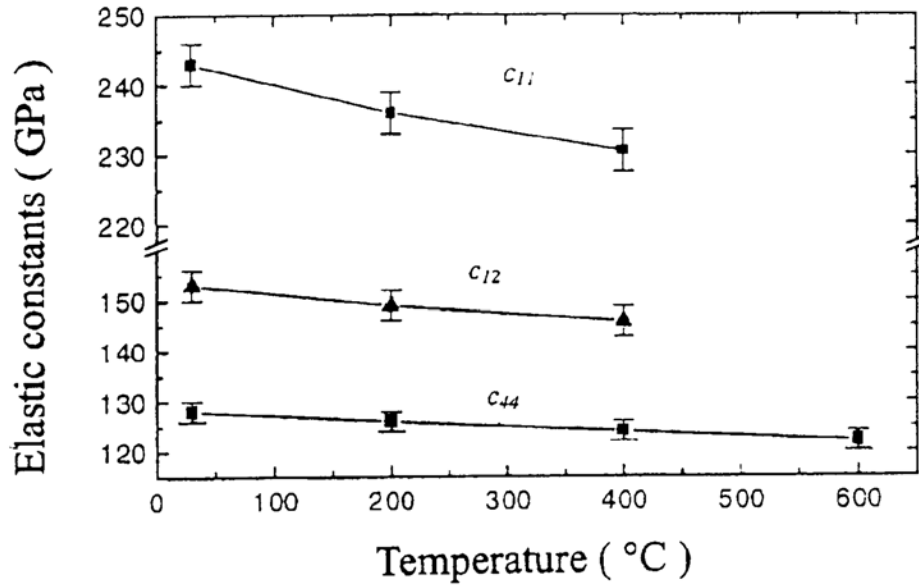


Fig. 6. The variation of the elastic constants with temperature for CMSX-4. The elastic constants display a nearly linear decrease with increasing temperature.

#### *Vanadium carbides*

Vanadium carbides  $VC_x$ , where  $x$  is the carbon-to-metal ratio have very high melting temperatures, hardness and high temperature strength, and have good electrical and thermal conductivity. These desirable properties make vanadium carbides suitable for high temperature applications and for components requiring high wear resistance. They have a wide range of composition ( $0.65 < x < 0.90$ ) while maintaining the cubic NaCl-type structure. Randomly distributed carbon vacancies from the changed carbon-to-metal ratio have a substantial effect on the elastic properties.

Measurements of the elastic constants by SBS for three different  $VC_x$  compositions were carried out by Zhang et al [15] using similar methods to those reported above for the CMSX-4 nickel-based superalloy. Rotation X-ray diffraction analysis of the three vanadium carbides investigated ( $VC_{0.88}$ ,  $VC_{0.84}$ , and  $VC_{0.75}$ ) showed a dominant pattern from the disordered phase in which the carbon vacancies are randomly distributed on the carbon lattice sites. Suitable samples were cut, oriented by Laue X-ray methods and mechanically polished to a surface finish of  $0.1 \mu\text{m}$  to provide the conditions for successful SBS measurements.

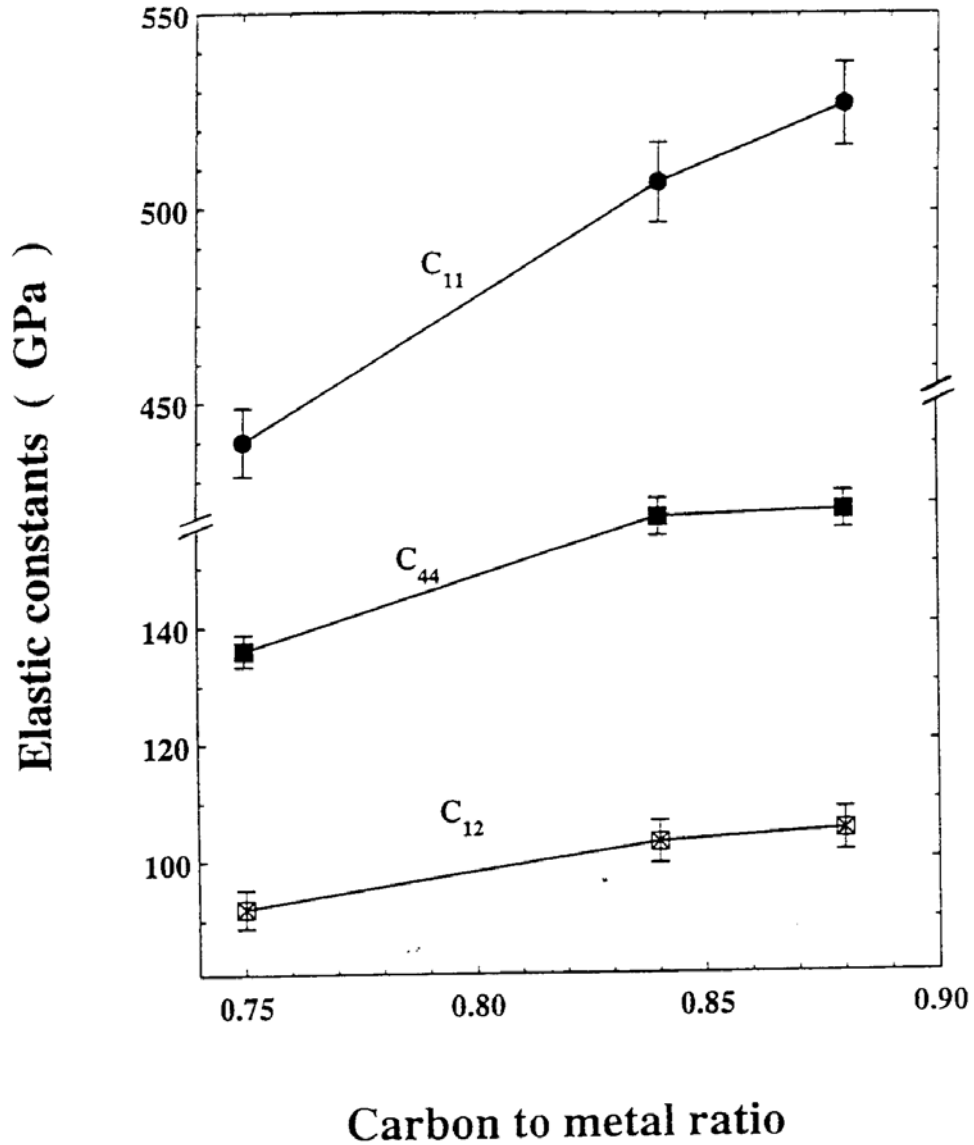


Fig.7. The variation of the elastic constants with carbon to metal ratio in vanadium carbides. The elastic constants decrease with reduction in the carbon to metal ratio.

The angular variation of the Rayleigh SAW velocity on the  $(100)$  and  $(1\bar{1}0)$  surfaces was measured for each of the three samples. From the SBS spectra for each of the samples, for surface wave-vector in the  $(110)$  direction on the  $(1\bar{1}0)$  surface, the minimum in the Lamb shoulder at the longitudinal threshold was determined. From these respective minima the combination  $(c_{11} + c_{12} + 2c_{44})$  could be determined for each of the vanadium carbides. By combining these data with that of the angular dispersion of the RW velocity, the least squares analysis showed a well-defined minimum for  $\chi^2$ . The overall results demonstrate the considerable variation of the elastic constants with composition as shown in Fig. 7. The Young's modulus ( $E$ ) and the shear modulus ( $G$ ) can be expressed as directionally dependent combinations of the tensor elastic constants [16]. From the measurements of the elastic

constants, the composition variation of  $E$  and  $G$  in the three high symmetry directions [100], [110] and [111] was obtained as shown in Fig. 8. Both  $E$  and  $G$  decrease with the reduction in carbon to metal ratio. For comparison, measured values of  $E$  and  $G$  for polycrystalline  $\text{VC}_{0.84}$  and  $\text{VC}_{0.83}$  are also shown using data from ref. [17].

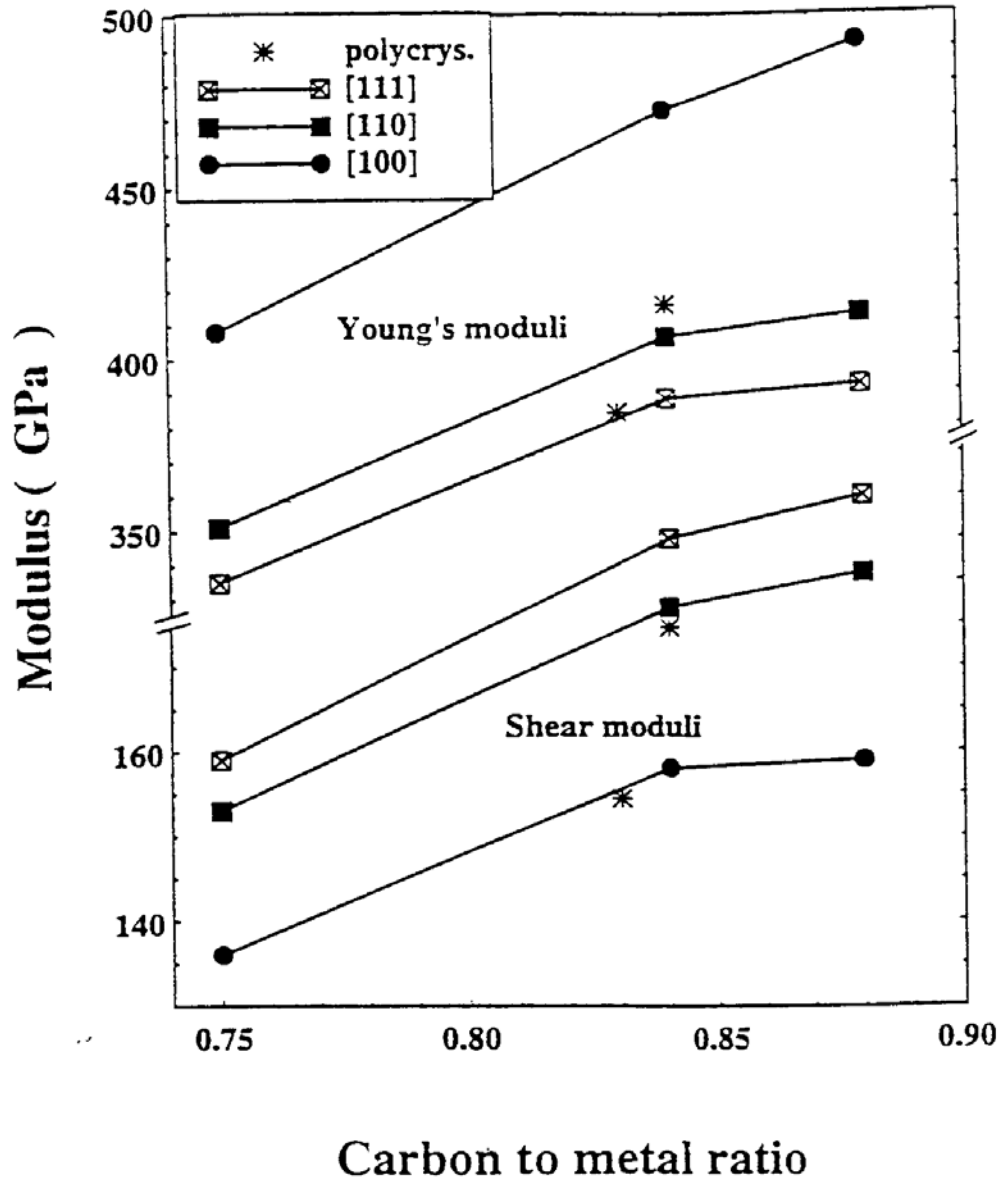


Fig.8. Variation of Young's and shear moduli with carbon-to-metal ratio in vanadium carbides.

#### *TiN on high speed steel*

TiN coatings on high speed steel (HSS) have important practical applications in cutting tools, and in the context of SBS investigations provide a "stiffening" situation in which the presence of the TiN film increases the SAW velocity over that of the substrate. This has been exploited in several publications by Pang et al. [18-21] concerned with theoretical and experimental studies on TiN films of various thickness deposited on HSS by magnetron sputtering.

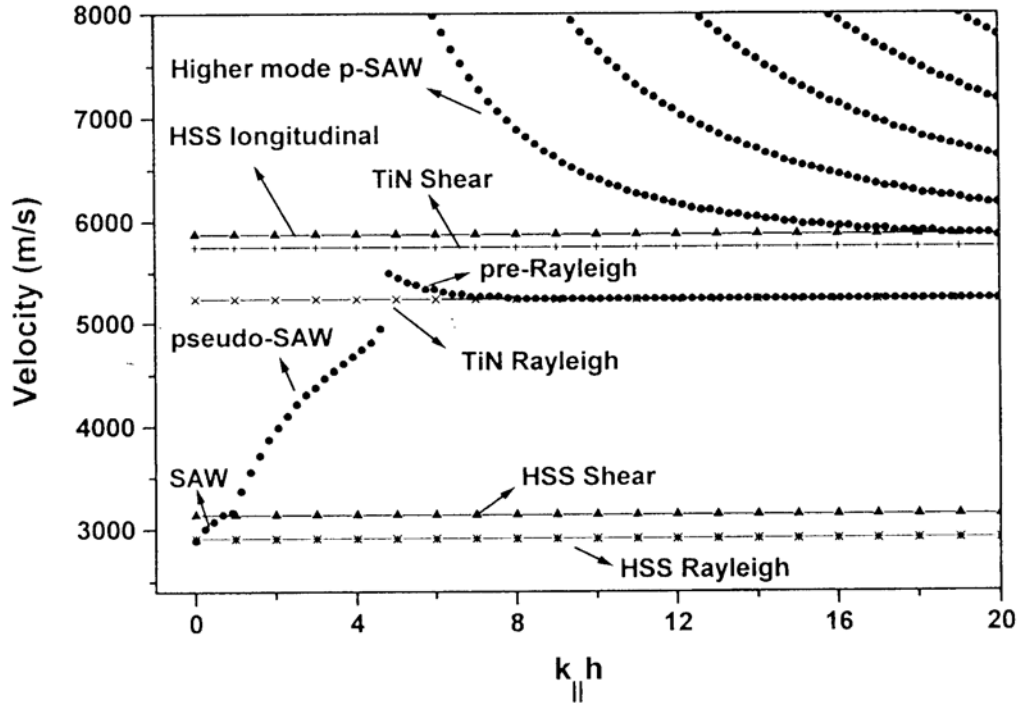


Fig. 9. Calculated dispersion curves of surface acoustic excitations in TiN on HSS. The shear velocity of TiN is 1.79 times that of HSS, so that TiN/HSS represents a strong stiffening system.

In these investigations, velocity dispersion curves were determined by SBS measurements for a range of TiN film thickness  $h$  (from 0 to 4180 nm), and hence  $k_{\parallel}h$ . The results calculated using the surface Green's function method use the Voigt/Reuss averaged elastic constants for a polycrystalline isotropic film and is presented in Fig. 9. This shows that with increasing film thickness, the SAW velocity increases from the RW velocity of the HSS substrate eventually attaining the RW velocity of the TiN film. Initially in the region  $0 < k_{\parallel}h < 0.8$ , there is a steady increase in velocity until the SAW degenerates with the bulk wave continuum at the shear wave threshold of the substrate (HSS shear) at  $k_{\parallel}h \approx 0.8$ . Within this region the surface mode is a true SAW, with the partial waves in the substrate falling off exponentially away from the surface, and  $|B|$  vanishing. For  $1 \leq k_{\parallel}h \leq 8$ , one of the partial waves in the substrate is a bulk wave and we have a highly-damped p-SAW. For  $k_{\parallel}h \geq 8$ , the surface mode is a p-SAW with lower damping that evolves into the RW for TiN at the larger values of  $k_{\parallel}h$ . There is a discontinuity in the dispersion curve for the p-SAW mode near  $k_{\parallel}h = 4.6$ . This discontinuity is present when the film provides sufficient stiffening. Higher order p-SAW modes are evident for sufficiently large values of  $k_{\parallel}h$ . Fig.10 shows the appearance of these various excitations by way of the calculated SBS spectrum and the SBS measurements. (Note that narrow peaks such as the RW are instrumentally broadened in the experimental spectra). Although good agreement is achieved using the accepted value of the elastic constants of TiN and HSS for the thicker films ( $h \geq 870$  nm), satisfactory agreement could only be achieved for the thinner films with significant reductions in the elastic constants of TiN.

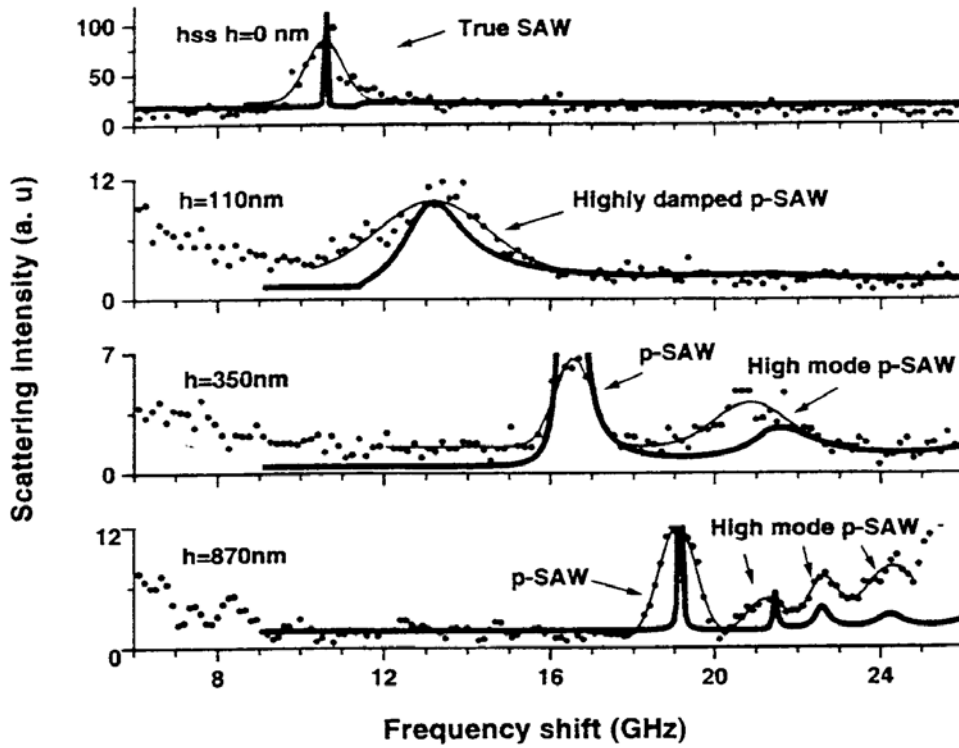


Fig. 10 Comparison between measured and calculated spectra of TiN/HSS for some typical TiN film thicknesses;  $h = 0$  nm, corresponding to the bare HSS substrate,  $h = 110$ , 350, and 850 nm. In the calculations, no adjustments of the elastic constants were made for the bare HSS substrate and for the 870 nm film. For the 110nm film the elastic constants of TiN were reduced to 60% of the bulk values, while for the 350 nm film a reduction to 75% was made.

Similarly it was found that while there was good agreement between the calculated and experimentally measured velocity dispersion curves over the ranges of larger TiN film thickness using the accepted values of the elastic constants of TiN, there was significant disagreement for the thinnest films. Subsequent XPS studies revealed the presence of a thin layer of TiO between the TiN film and the HSS substrate. Such an oxide layer is expected to have significantly lower elastic constants than TiN. As an approximation to the effects of the elastically softer layer, a comparison was made between the measured and calculated wave velocities of TiN/HSS as a function of film thickness for the thinner TiN films; here the elastic constants for the TiN film were reduced to 75% of the values for bulk TiN. Fig. 11 shows that this procedure yield quite good agreement for the pure SAW, p-SAW and the first higher order p-SAW mode. The fact that the SAW velocities are reduced most strongly for the thinner films is consistent with the presence of the interface layer, since this occupies a larger fraction of the volume of the total overlayer. The results demonstrate that discrepancies between experimental and theoretical SBS spectra, can reveal the presence of unexpected features of a system.

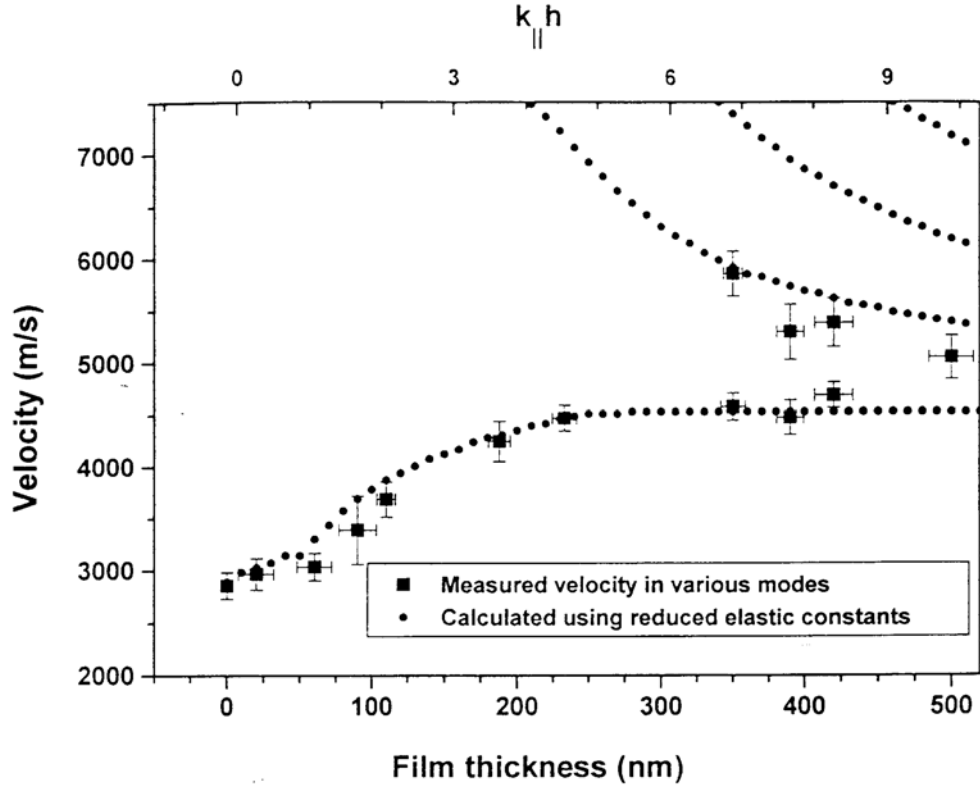


Fig. 11. Comparison between the measured and calculated wave velocities of TiN/HSS as a function of film thickness (bottom axis) and  $k_{\parallel}h$  (top axis). The calculations assume elastic constants for the film which are 75% of the values for bulk TiN. For film thickness  $h = 870$  nm (not included in the figure), the measured results conform rather well to the calculated ones based on elastic constants of bulk TiN. Lower curve: Rayleigh SAW and p-SAW; upper curve: higher order p-SAW modes.

#### *Ion-bombarded silicon*

There has been considerable interest in the area of elastically softer films on harder substrates in which the SAW velocity is decreased with respect to that of the substrate. Where the transverse bulk wave velocity in the layer  $V_t^l$  is smaller than that in the substrate  $V_t^s$ , and for a limited range of  $k_{\parallel}h$ , additional true surface modes named Sezawa waves are drawn out from the continuum of surface excitations. They have particle displacements that are mainly localised in the film, falling off exponentially into the substrate.

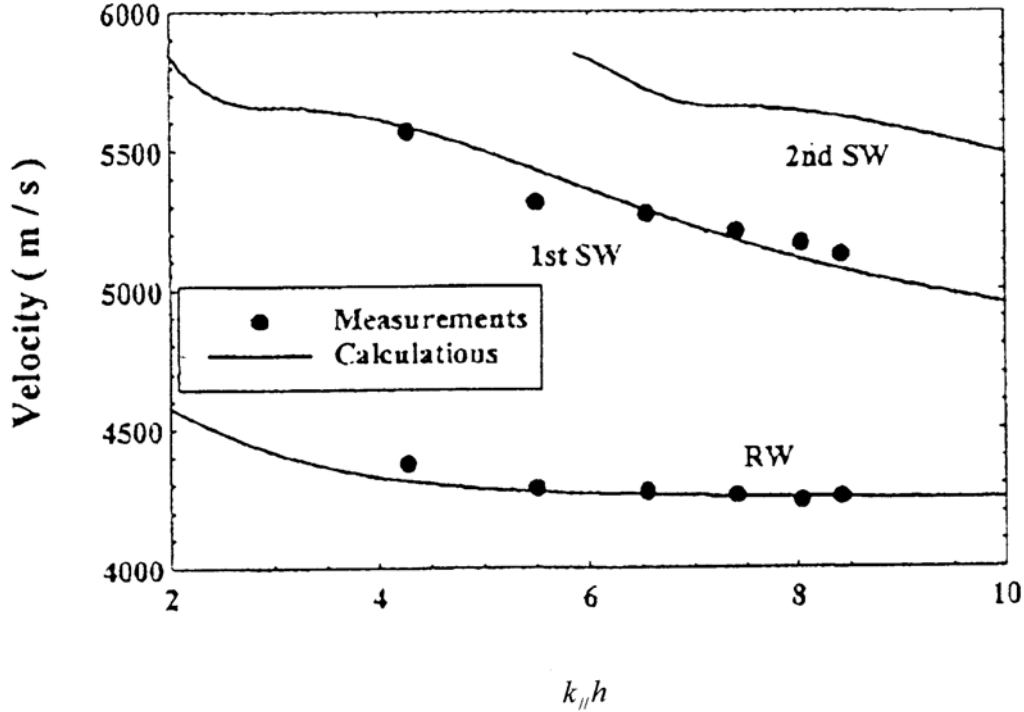


Fig. 12. The measured and calculated velocity dispersion curves of SAW modes in the carbon ion bombarded sample. The measurements are in agreement with the calculations for both the Rayleigh (RW) and the first order Sezawa SAW (SW).

Zhang et al. [7,11] have carried out SBS experiments by on crystalline silicon bombarded with argon and carbon ions. As an illustration we shall discuss the carbon ion bombardment carried out with energy 100 keV and fluence of  $1 \times 10^{17}$  ions/cm<sup>2</sup>. This created a completely amorphised layer on the (001) silicon surface as confirmed by Raman spectroscopy with the complete suppression of the strong Raman peak of crystalline silicon near 520 cm<sup>-1</sup>. By means of a TRIM simulation of the ion-bombardment process [22] the layer thickness  $h$  was estimated as 360 nm. In the calculation of the velocity dispersion relations, the system was modelled as a single amorphous silicon layer of this thickness on a crystalline silicon substrate. The calculated surface wave velocities were determined from the combined elastic properties of the silicon substrate and the layer using the surface Green's function method. The best fit values of the elastic constants for the amorphous silicon layer are  $c_{11} = 143$  GPa and  $c_{44} = 49.6$  GPa. The measured and calculated velocity dispersion curves are shown in Fig. 12. The system of amorphous silicon on silicon satisfies the conditions for the appearance of Sezawa waves. Fig. 12 also shows the velocity dispersion of the measured first order Sezawa waves. There is good agreement between the calculations and experiment.

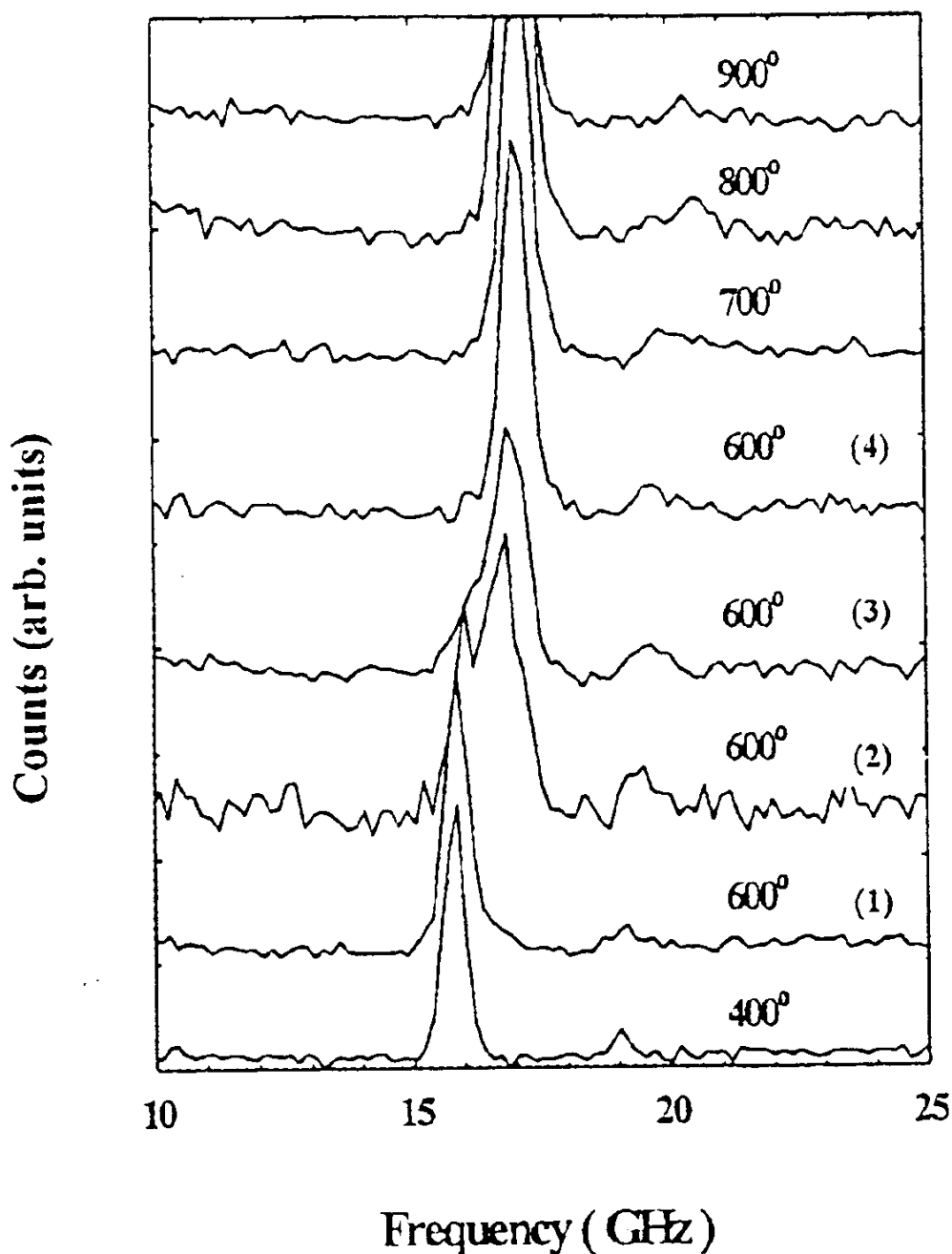


Fig. 13. The anti-Stokes SBS spectra for the carbon ion bombarded sample taken along the [100] direction referred to the (001) silicon substrate at different temperatures. At 600 °C, a broadened peak was observed in the second measurement, indicating a structural transition had occurred.

As a further part of this study, the structure of the layer produced by the ion bombardment during annealing to high temperatures was examined by *in situ* by SBS. The carbon-ion bombarded sample was progressively annealed at high temperatures in an optical furnace at a series of temperatures from room temperature to 900 °C. At each temperature, several SBS measurements were made, each taking 20 min. The procedure was continued at a particular



temperature until the observed SAW peak did not change in position. Fig. 13 shows the anti-Stokes SBS spectra for the sample taken along the [100] direction referred to the (001) crystalline silicon surface at each annealing temperature. The last spectrum at each temperature is shown (except for those at 600 °C) since it gives the stable SAW peak for that temperature. From the behaviour of the Rayleigh SAW peak at 600 °C, it is evident that a structural transition takes place which alters the elastic properties of the layer. Spectra obtained at yet higher temperatures are only slightly different from the final spectrum obtained at 600 °C. Fig. 14 shows the velocities of the Rayleigh SAW for the last stable spectrum at each temperature. There is a steady increase in velocity between ambient and 400 °C, in contrast to high temperature SBS results on crystalline silicon [8]. A significant increase in SAW velocity occurs at 600 °C. Post-annealing Raman spectra showed that the crystalline silicon Raman peak is recovered. The peak had a larger width and was of somewhat lower intensity indicating the re-crystallised silicon is not as perfect as the original single crystal. The recovery of the Rayleigh SAW velocity is substantial and is considered to result mainly from this re-crystallisation process during annealing. The work demonstrates the potential of SBS for the *in situ* monitoring of structural phase transitions in opaque materials.

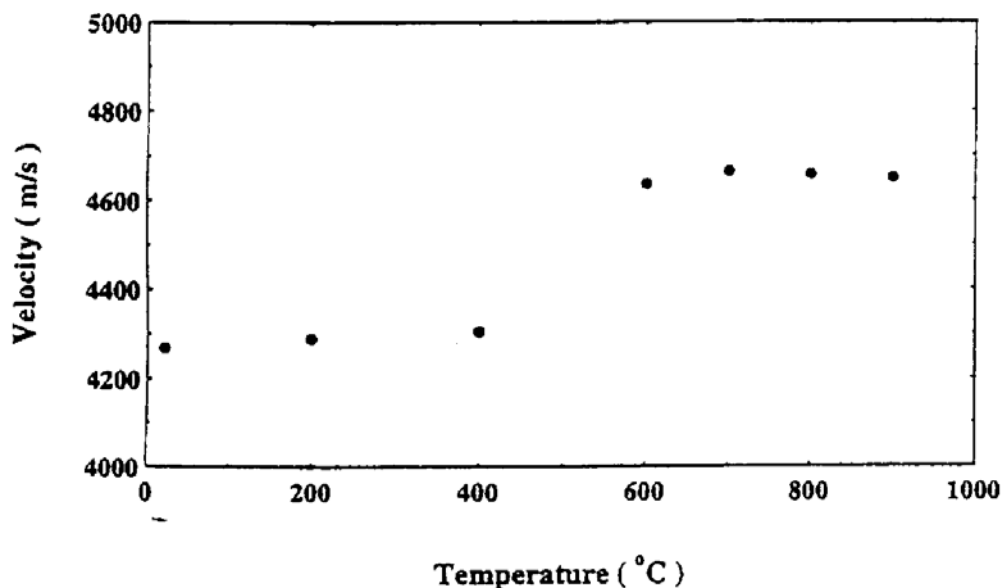


Fig. 14. The velocity of the Rayleigh SAW measured by the last stable spectrum at each temperature during annealing of the sample of carbon bombarded silicon.

### Acknowledgements

We wish to thank the National Research Foundation, South Africa for financial support.

### References

- [1] F. Nizzoli and J. R. Sandercock, in: G. K. Horton, A. A. Maradudin (Eds.), *Dynamical Properties of Solids*, Vol. 6; *The Modern Physics of Phonons: Transport, Surfaces and Simulations*, North Holland, Amsterdam, Ch. 5, p. 281.
- [2] P. Mutti, C. E. Bottani, G. Ghislotti, M. Beghi, G. A. D. Briggs, J.R. Sandercock, in: A. Briggs (Ed.), *Advances in Acoustic Microscopy*, Vol. 1, Plenum, New York, 1995, p. 249.
- [3] J D Comins, A G Every, P R Stoddart, X Zhang, J C Crowhurst, and G R Hearne, *Ultrasonics* **38** (2000) 450.
- [4] J D Comins, "Surface Brillouin Scattering", in the *Handbook of Elastic Properties of Solids, Liquids and Solids*, eds. M Levy, H Bass and R Stern, Volume 1. Methods for

- Measuring the Elastic Properties of Solids, eds. A G Every and W Sachse, Chapter 15, Academic Press, New York, 2001, p349.
- [5] R. Loudon, Phys. Rev. Lett. 40 (1978) 581.
  - [6] V. Bortolani, F. Nizzoli, G. Santoro, Phys. Rev. Lett. 41 (1978) 39.
  - [7] X. Zhang, J. D. Comins, A. G. Every, P.R. Stoddart, W. Pang and T.E. Derry, Phys. Rev. 58 (1998) 13677.
  - [8] P. R. Stoddart, J. D. Comins, A. G. Every, Phys. Rev. B 51 (1995) 17574.
  - [9] P. R. Stoddart, J. D. Comins, A. G. Every, Physica B 219 and 220 (1996) 717.
  - [10] X Zhang, P R Stoddart, J D Comins and A G Every, J. Phys: Condens. Matter **13** (2001) 1
  - [11] X Zhang, J D Comins, A G Every and T E Derry, Phys. Rev. B, **65** (2001) 012106-1
  - [12] J C Crowhurst, G R Hearne, J D Comins, A G Every and P R Stoddart, Phys. Rev. B **60** (1999) R14990
  - [13] P. R. Stoddart, J. C. Crowhurst, A. G. Every, J. D. Comins, J. Opt. Soc. Am. B15 (1998) 2481.
  - [14] G. W. Farnell, in: W. P. Mason, R. W. Thurston (Eds.), Physical Acoustics, Vol. 6, Academic, New York, 1970, p.109.
  - [15] X. Zhang, J. D. Comins, A.G. Every and P. R Stoddart, Int. J. Refrac. Metals Hard Mater. 16 (1998) 303.
  - [16] E. Schmidt and W. Boas, Plasticity of Crystals, Hughes, London, 1950, p14.
  - [17] R.H.J. Hannink and M.J. Murray, J. Mater. Sci. 9 (1974) 223.
  - [18] W Pang, P R Stoddart, J D Comins, A G Every, D Pietersen and P J Marais, Int. J. Refract. Met. Hard Mater., 15 (1997) 179.
  - [19] A G Every, W Pang, J D Comins and P R Stoddart, Ultrasonics 36 (1997) 223.
  - [20] J D Comins, W Pang, A G Every and D Pietersen, Int. J. Refract. Met. Hard Mater. **16** (1998) 389.
  - [21] W Pang, A G Every, J D Comins, P R Stoddart and X Zhang, J. Appl. Phys. **82** (1999) 311-317.
  - [22] J. F. Ziegler, J. P. Biersack, and U. Littmark, The Stopping and Range of Ions in Solids, Pergamon, New York, 1985.